Experimental tests on double-resolution coherent imaging via STEM

J.M. Rodenburg, B.C. McCallum and P.D. Nellist

Cavendish Laboratory, University of Cambridge, Madingley Road, Cambridge CB3 0HE, UK

Experimental data collected in a scanning transmission electron microscope (STEM) is used to obtain an image of the specimen at twice the conventional resolution determined by the size of the objective aperture. The measured data also provide a robust estimate of the quality of the reconstruction, determining such variables as specimen drift, defocus in the objective lens, source coherence and mechanical instability.

1. Introduction

We aim to improve the resolution of the electron microscope without recourse to further reduction of the electron wavelength or the spherical aberration constant of the objective lens. It has been shown both theoretically [1–3] and experimentally on the optical bench [4,5] that if a sufficiently redundant data set is processed consisting of either (i) all coherent microdiffraction patterns available in the scanning transmission electron microscope (STEM) collected as a function of many equally spaced probe positions, or (ii) all coherent bright- and dark-field images available in the conventional transmission electron microscope (CTEM) collected as a function of many equally spaced illumination-angle conditions, then it is possible to remove all the degrading transfer characteristics of the objective lens and solve for the exist wavefunction from the specimen in complex amplitude at much improved resolution. In this paper we present initial results from a STEM implementation of the method, and show that when the specimen is weakly scattering, we can easily observe an equivalent to the conventional contrast transfer function (though now in four dimensions) and thus test for the experimental parameters such as specimen drift, lens defocus and source coherence. In theory, we can obtain an unaberrated image without any knowledge of defocus, spherical aberration or astigmatism present in the objective lens. However, reliance on the particular theoretical nicety which gives this "lens-insensitive" solution may be rather hazardous because it assumes the objective lens is well aligned with the optic axis, and it is also wasteful of electron counts. More satisfactory results may be obtained by performing a full Wigner distribution deconvolution [2]. The extreme redundancy in the measured data allows for the more general possibility of developing a robust, "user-independent" form of computational high-resolution electron microscopy.

2. Apparatus

We employ a VG Microscopes HB501 STEM in the optical configuration shown schematically in fig. 1. 100 keV electrons (wavelength $\lambda = 0.0037$ nm) from a high-brightness field-emission gun are focused into a tight (though possibly aberrated) electron probe in the specimen plane by an objective lens (spherical aberration constant of 3.1 mm) which has a small (4–8 mrad semi-angle) objective aperture positioned in its back-focal plane. The transmitted electrons are brought to a focus at the slits of a magnetic spectrometer to remove those which have lost more than 1 eV,

and the resulting angularly resolved distribution is recorded on a TV-rate CCD camera (with an 8-bit dynamic range) via a thin YAG scintillator bonded to an optical fibre, which also acts as the vacuum feedthrough. A set of three quadrupoles (usually employed for setting the energy dispersion of the parallel EEL spectrometer) are used to alter the magnification of the distribution with respect to the pixel sampling in the CCD camera [6]. With this arrangement, we can adjust defocus and astigmatism in the objective lens by observing the shadow image and, at the same time, correct for the aberration figure of the spectrometer. A typical energy-resolved shadow image is shown in fig. 2 To improve the spatial coherence of the optics, we run the second condenser lens as high as possible (typically three coarse stops above the selected-area aperture cross-over), but this setting must compete with the resulting loss of electron counts.

The crucial property of the processing method described below is that data are collected for many positions of the electron probe, each sampled from an evenly spaced grid of points in the specimen plane separated by a distance of the order of 0.1 nm. Our main experimental difficulty is specimen drift, which is typically of the order of
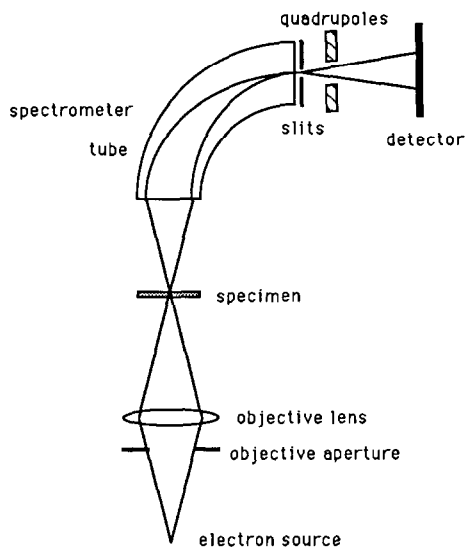
0.5 nm per minute, and so it is important that data are collected and stored quickly. In these preliminary experiments, we record the electron distribution on a 64×64 pixel frame, for 32×32 probe positions in 80 s, during which the specimen may drift significantly. We therefore drive the position of the probe via 16-bit D/A converters which can be programmed to correct dynamically for a constant drift rate. Each microdiffraction pattern is shifted in real time, via an Imaging Technology 151 frame-grabber, into the memory of a SUN workstation using a VME data bus. Before being written to disc (when the experiment is completed), each microdiffraction pattern is summed into 32×32 pixels, to avoid unevenness in the interlaced TV signal. All experiments are duplicated (the probe is immediately rescanned over the same area, while collecting a second set of data) to check both that the drift rate has not changed during the experiment and that the reconstruction is reproducible.

The objective aperture was accurately aligned onto the optic axis by positioning it on the centre of zoom of the shadow image which is formed on the CCD camera when the probe is significantly defocused. Defocus was then finely adjusted until there was no obvious preferential movement in the shadow image while the probe was scanned slowly across the specimen. The reconstruction method employed below is not very sensitive to defocus. It can be helpful, though, to have some defocus, so that the contrast in the bright-field image can be used to estimate the drift rate. The specimen used in these experiments was thin amorphous carbon which may be presumed to contain a broad distribution of spatial frequencies, as often employed in the measurement of the conventional contrast transfer function [7].

Fig. 1. A schematic diagram of the STEM configuration used for the experiments.

3. Four-dimensional complex transfer function

Following the nomenclature in earlier work [1,2], let ρ be a two-dimensional vector describing the position of the probe in the specimen plane and r' be a two-dimensional vector describing a position in the Fraunhofer diffraction plane (i.e. a particular CCD pixel in the microdiffraction

plane). We have recorded a four-dimensional intensity data set which we call $|M(r', \rho)|^2$. If we were to examine a slice through $|M(r', \rho)|^2$ at constant r', we would see a conventional image mapped out as a function of the probe position ρ. For example, if $r' = 0$, we would see the conventional axial bright-field image. Now it is well known that the Fourier transform of a conventional image gives a "diffractogram" which indicates the band pass of the objective lens (assuming the specimen is a weak phase object). However, now let us consider the set of all such diffractograms, namely the Fourier transform of $|M(r', \rho)|^2$ with respect to the ρ coordinate, which we will call $G(r', \rho')$, such that

$$G(r', \rho') = \int |M(r', \rho)|^2 \exp(i2\pi\rho \cdot \rho') \, d\rho,$$

(1)

where ρ' is the reciprocal coordinate of ρ. The scaling between r' and ρ' will depend on the electron wavelength and the effective camera length of our experimental arrangement, but we will show below that this can be determined directly from the data set itself.

With reference to the conventional transmission electron microscope (CTEM) literature, a tilted illumination diffractogram obtained when using an objective aperture and a thin specimen is known to give a magnitude distribution reminiscent of two apertures displaced with respect to one another (see refs. [8,9] and the auto-alignment literature, for example ref. [10]). It should be emphasized that here we process the complex value of $G(r', \rho')$ (though note that $G(r', \rho') = G^*(r', -\rho')$), whereas diffractograms have historically been recorded on the optical bench, thus yielding $|G(r', \rho')|^2$. The reason these displaced
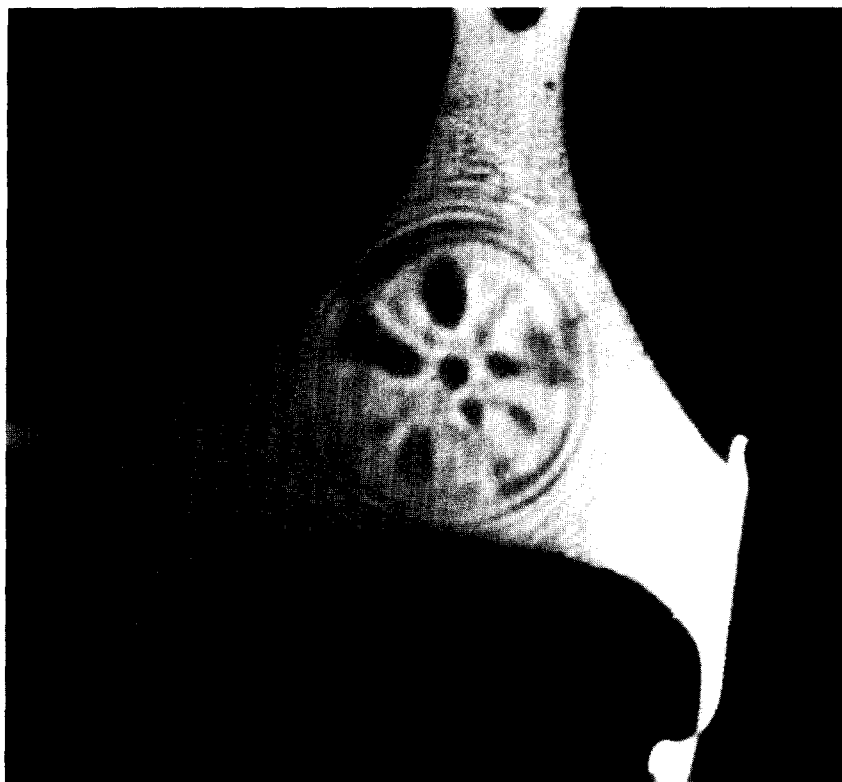

Fig. 2. A typical energy-resolved shadow-image of evaporated gold islands on a carbon support film. The very intense region at the edge is caused by high-angle beams being mapped back to lower angles by the spectrometer aberration. The use of an objective aperture blocks intense high-angle beams, and since we only process the zero-order microdiffraction disc we are not affected by the aberration figure.

apertures appear can be most easily understood as oblique incidence holography [11], because the Fourier transform of the intensity of the conventional image is the autocorrelation of the wavefield in the back-focal plane, and so if the unscattered beam is strong (that is to say the specimen is weak phase) and tilted, the two sidebands become separated. Filtering one such sideband with the complex transfer function of the lens, and then Fourier-transforming back to the image plane, can give a double-resolution image in complex amplitude, as demonstrated by Hohenstein [12,13], provided one is confident that the lens properties are known accurately. However, in this experiment we have effectively collected all such possible illumination conditions, and this extra information can be used (i) to check the stability of specimen and microscope, (ii) to check the lens parameters actually contributing to the experiment, (iii) to check that the specimen really is a weak phase scatterer, (iv) to check the coherence properties of the source, and (v) if the specimen is strong (but still reasonably thin) to deconvolve via the Wigner distribution method [2].

Let us first assume that the specimen is weak, so that under plane wave illumination conditions, the wavefield at the exit surface of the specimen would be

$$\psi(r) = 1 - \mathrm{i}f(r), \quad |f(r)| \ll 1, \quad (2)$$

where r is a two-dimensional vector in the specimen plane, and where $f(r)$ is real, much smaller than unity, and is proportional to the projected atomic potential (see, for example, ref. [14]). For some general $\psi(\bar{r})$, $M(r', \rho)$ is given by a convolution of the coherently illuminated aperture function lying in the back-focal plane of the lens, which we denote $A(r')$, with $\Psi(r')$ the Fourier transform of $\psi(r)$, such that

$$|M(r', \rho)|^2$$

$$= \int\!\!\int A(b')\Psi(r'-b')A^*(c')\Psi^*(r'-c')$$

$$\times \exp[\mathrm{i}2\pi\rho \cdot (b'-c')] \, \mathrm{d}b' \, \mathrm{d}c', \quad (3)$$

where the probe position ρ has been explicitly included, and b' and c' are the dummy variables

of the convolution. $A(r')$ may be a complex quantity, depending on aberration, astigmatism and defocus. If $\psi(r)$ satisfies (2), $\Psi(r')$ is of the form

$$\Psi(r') = \delta(r') + \Psi_s(r'), \quad (4)$$

where $\delta(r')$ is a delta function representing the unscattered beam, and $\Psi_s(r')$ is the scattered wave given by

$$\Psi_s(r') = -\mathrm{i}F(r'), \quad (5)$$

where $F(r')$ is the Fourier transform of $f(r)$ defined as

$$F(r') = \int f(r) \exp(\mathrm{i}2\pi r \cdot r') \, \mathrm{d}r. \quad (6)$$

It is useful to note that, because $f(r)$ is real, $F(r') = F^*(-r')$, and hence

$$\Psi_s(r') = -\Psi_s^*(-r'). \quad (7)$$

From eqs. (1), (3) and (4), for a weak phase object

$$G(r', \rho') = |A(r')|^2\delta(\rho')$$
$$+ A(r')A^*(r'+\rho')\Psi_s^*(-\rho')$$
$$+ A^*(r')A(r'-\rho')\Psi_s(\rho'), \quad (8)$$

where we have ignored cross-terms between the scattered parts, $\Psi_s(r')$.

If the function $A(r')$ has a circular stop (the objective aperture), of semi-angle α, then $G(r', \rho')$ contains significant magnitude in the regions illustrated schematically in fig. 3. Fig. 3a is a plot through $G(r', \rho')$ along one component of the two-dimensional vector r' and the corresponding parallel component of ρ', the remaining components of both r' and ρ' being zero. A plane through $G(r', \rho')$ for constant r' (represented by a vertical line in fig. 3a) will have the form illustrated in fig. 3b, the tilted beam diffractogram discussed above. As r' increases, the two circles in the diffractograms, which are plotted as a function of ρ', are seen to separate. Meanwhile, the magnitude of a plane represented by a horizontal line in fig. 3a (i.e. $G(r', \rho')$ plotted as a function of r' for a constant value of ρ') will have significant value where the fixed central disc (the superposition of the $A(r')$ and $A^*(r')$ terms

☑ Ψₛ transferred with unity magnitude
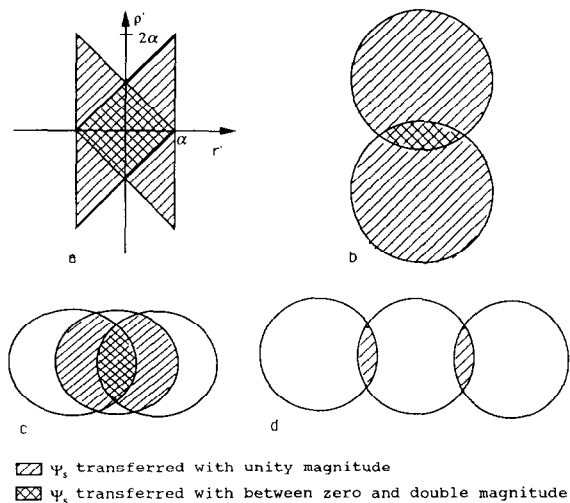☒ Ψₛ transferred with between zero and double magnitude

Fig. 3. Regions of significant magnitude in $G(r', \rho')$: (a) along corresponding parallel components of r' and ρ', the remaining components of both r' and ρ' are zero; (b) as a function of ρ' for a constant r'; (c) as a function of r' for constant ρ' ($|\rho'| < \alpha$); (d) as a function of r' for constant ρ' ($\alpha < |\rho'| < 2\alpha$).

in eq. (8)) is overlapped by two other discs (the $A(r' + \rho')$ and $A(r' - \rho')$ terms in eq. (8)) which, as ρ' increases, will be seen to move apart from one another, as shown in figs. 3c and 3d. We call these shapes "aperture offset functions". In fact, when these two outer discs overlap each other at small values of ρ', they may contain regions which transfer $\Psi_s(r')$ with between zero or double amplitude depending on the exact phase of the objective lens transfer function, $A(r')$. For example, for a perfect lens (no phase change across the aperture) $\Psi_s^*(-r')$ cancels with $\Psi_s(r')$ in the overlap region because of eq. (7). It is well known that in conventional bright-field phase-contrast imaging, it is ideal that the transfer function should introduce a $\pi/2$ phase change into both the scattered terms in order that they are expressed with double amplitude in the Fourier transform of the image.

The reconstruction method described below is easiest to perform when the second two terms in eq. (8) do not overlap. In fact, even if there is no aperture, these terms can be separated because the attenuation of the transfer function can be used as an effective aperture. However, the optimal conditions for this separation is an intricate function of defocus and the CCD pixel size in the microdiffraction plane, and so will be the subject of further investigation. We report here the main characteristics of $G(r', \rho')$ only in the simpler case in which an objective aperture is used.
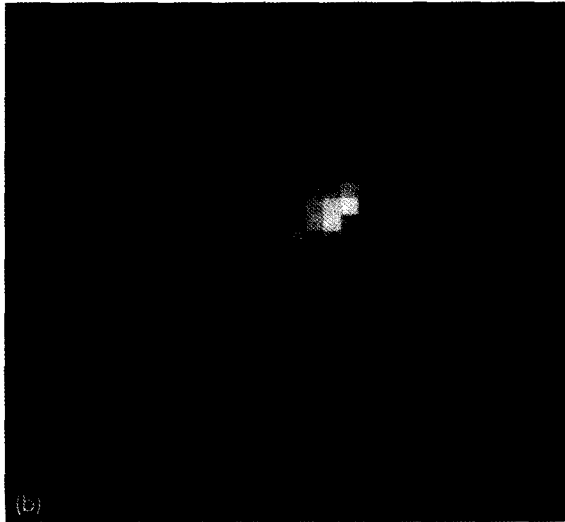

Fig. 4. (a, b) Axial bright-field images recorded consecutively. Note that the data set has been windowed in all the ρ planes to reduce edge effects in its Fourier transform $G(r', \rho')$. The greyscale spans the range 0.7 (black) to 1.0 (white).

4. Self-consistency tests on the experimental data

We now demonstrate that all the above features can be observed directly in the experimental data and can be used to test various alignment parameters in the microscope. Fig. 4 shows two conventional bright-field images, i.e. two sets of the data $|M(0, \rho)|^2$, recorded consecutively, as described above. The sampling in real space was 0.19 nm, the objective aperture used was 25 μm (a semi-angle of 4 mrad), hence the total field of view was 6.1 nm, with a nominal resolution of 0.93 nm. We may infer from the similarity of these two images that the specimen has not drifted with respect to the notional position of the probe (though in fact in these particular data we were compensating in real time for an actual drift rate of 0.3 nm per minute). Fig. 5 shows the central disc from one particular microdiffraction pattern, namely a slice through $|M(r', \rho)|^2$ at one particular ρ, displayed as a function of r'. Now let us take a Fourier transform with respect to ρ and look at the magnitude of slices in $G(r', \rho')$, plotted as a function of r' at increasing values of constant ρ' (figs. 6a–6c). The aperture offset

functions are clearly visible. Of course, they do not occur at all values of ρ' with equal strength because they depend upon the amplitude of the corresponding value of $\Psi_s(\rho')$, but for an amorphous specimen, they appear in most regions of $G(r', \rho')$.

We have observed that if the experimental conditions are unfavourable, the aperture offset functions are distorted, or simply not visible, and may therefore be used to determine the following experimental parameters.

Relative sampling: Scaling the position of a particular CCD element in r' to the reciprocal of probe movement ρ' is experimentally rather difficult. Depending on the specimen height, stray magnetic field from the objective lens alters the effective camera length between the specimen and the spectrometer. This is further exacerbated by our use of quadrupoles to demagnify the pattern after the spectrometer. However, simply by observing the relative movement of the aperture offset functions, we immediately obtain an accurate calibration of r' to ρ', without any knowledge of the camera length or even the electron wavelength.

Distortions in sampling: If the microdiffraction plane is rotated relative to the probe scan coils, the aperture offset functions in figs. 6a–6c are systematically rotated throughout $G(r', \rho')$. We have found that we normally have to correct for this computationally (by performing a rotated interpolation), firstly because the "rotate" adjustment on our HB501 is somewhat coarse, and secondly, aligning the scan by eye via a defocused shadow image (by observing the direction of its movement as the probe performs a line scan) is highly sensitive to any residual astigmatism. Any distortions in the microdiffraction plane caused by unequal excitations of the quadrupoles are easy to observe if one (perhaps rashly) assumes the objective aperture is circular. Continuous specimen drift stretches and distorts the sampling in ρ, and this manifests itself as aperture offset functions in r' that move at different rates as a function of ρ' in orthogonal directions. More catastrophic failures in sampling, such as a jump in the specimen position due to charging, or
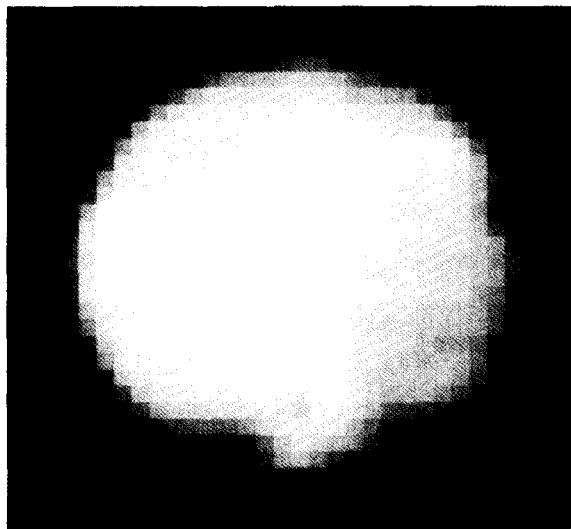

Fig. 5. The central (zero-order) disc from one particular microdiffraction pattern, i.e. a plot of $|M(r', \rho)|^2$ as a function of r' at constant ρ.

accelerating specimen drift, give highly distorted and blurred aperture structures.

Lens defocus and aperture position: The magnitude of the separated aperture features shown in fig. 6 are unaffected by phase changes across $A(r')$. (Strictly speaking, this is only true if the pixel size in r' is negligibly small. Finite pixel size

is equivalent, via reciprocity, to beam divergence in CTEM, which causes an attenuation in the transfer of high spatial frequencies.) However, the smoothness of the phase of the separated disc features shown in figs. 6b and 6c gives a very good indication of whether or not the probe was well focused during the experiment. A rapid phase change across $A(r')$, caused by spherical aberra-

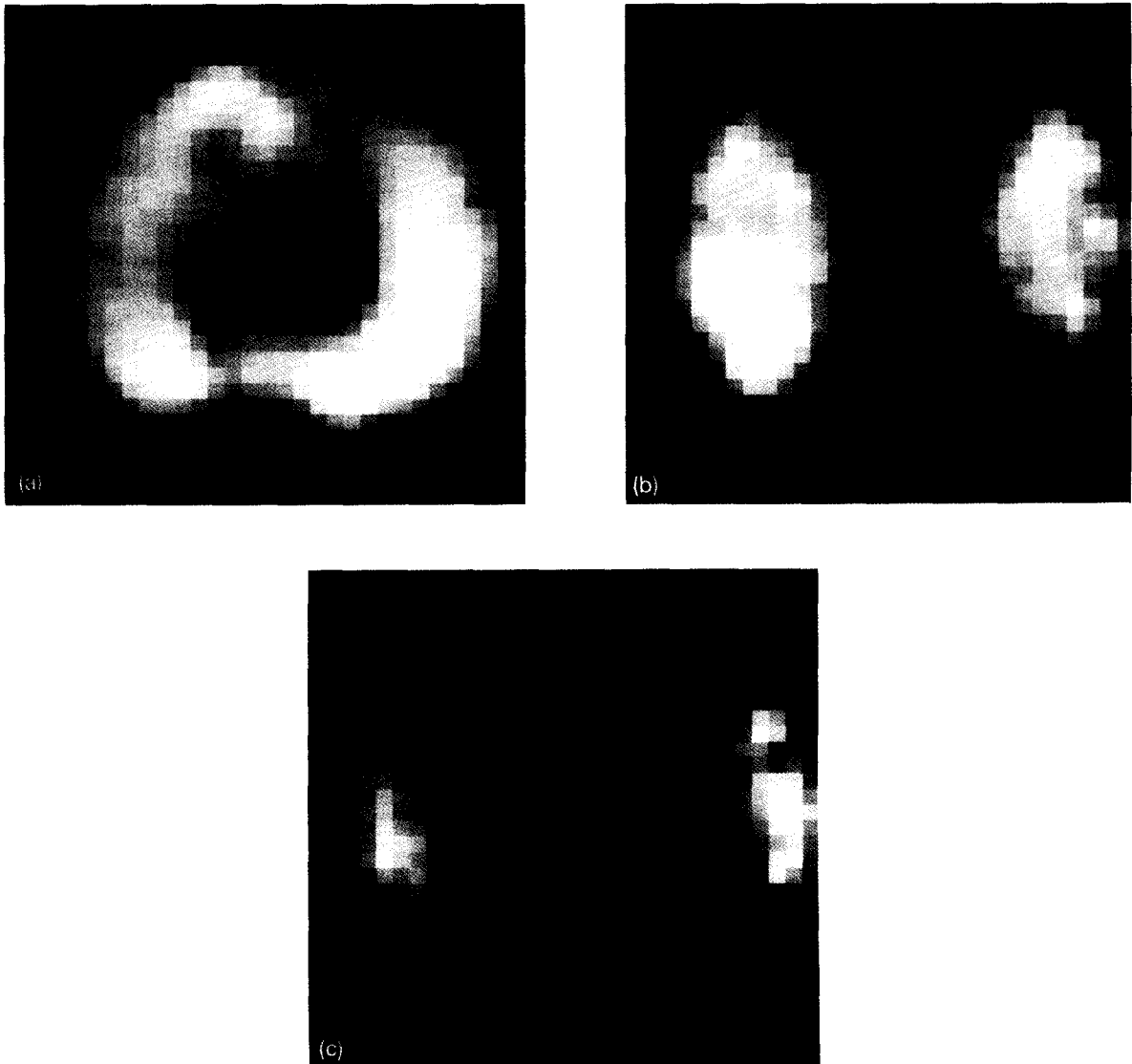Fig. 6. Plots of $|G(r', \rho')|$ as a function of r' for various ρ' values. The aperture offset functions can be seen to separate and move apart. (a) $|\rho'| = 0.6\alpha$; (b) $|\rho'| = 1.2\alpha$; (c) $|\rho'| = 1.5\alpha$.

tion or defocus, manifests itself as a phase gradient across the pairs of aperture terms in eq. (8). (We note in passing that corresponding points inside the two parts of the aperture offset functions are always π out of phase if the specimen is weak, via eqs. (7) and (8), as can be seen in fig. 8b which is discussed later.) In fact, assuming the specimen is weak, exploiting the full dimensionality of our data will almost certainly uniquely

define the lens parameters, for example by performing the type of analysis suggested by Typke and Köstler [9], or more generally for a strong object and arbitrary lens function, by solving the blind deconvolution problem iteratively [15,16].

Source coherence: The magnitude of the signal in the offset aperture functions at high values of ρ' gives a measure of the total source coherence,
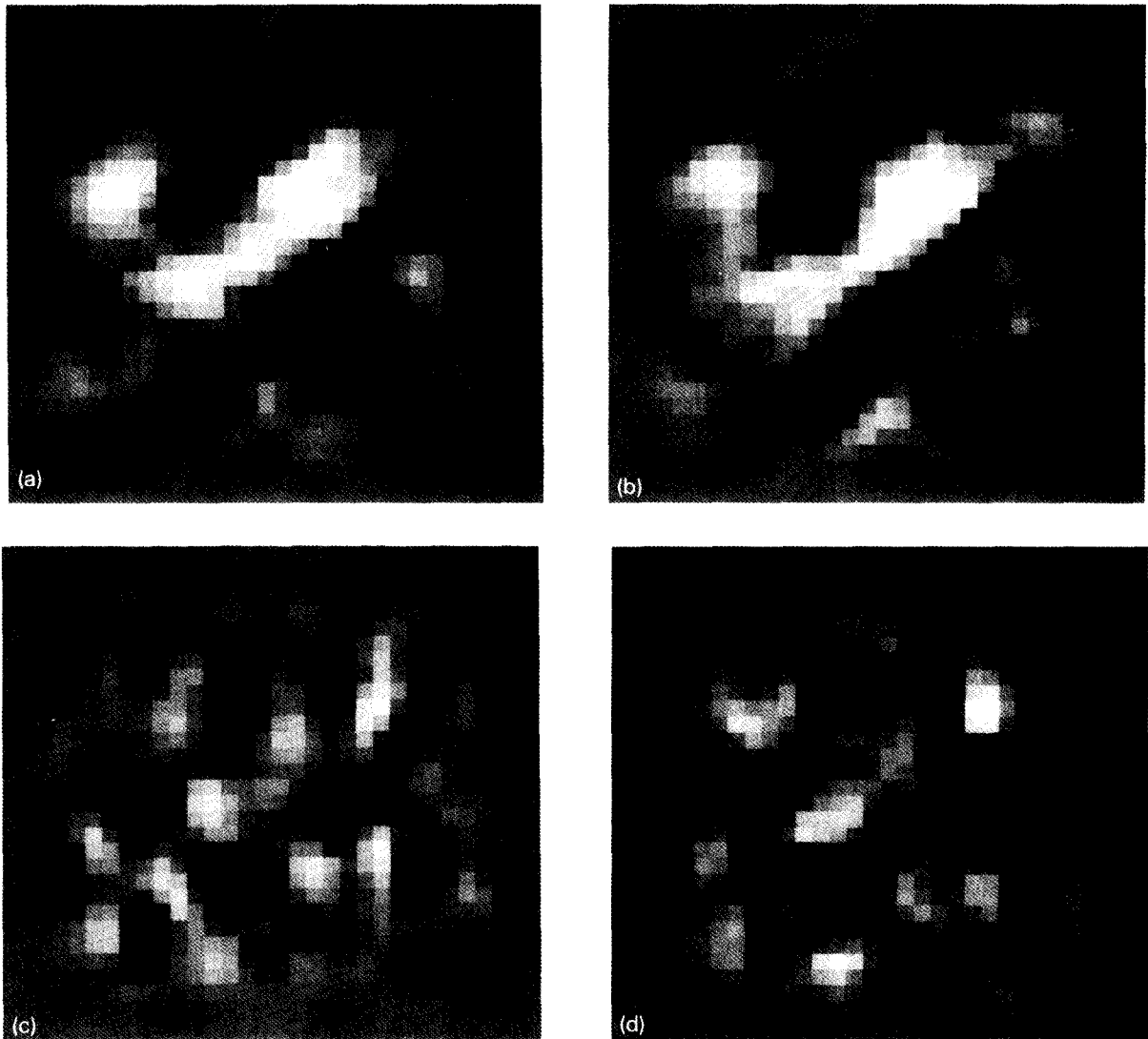

Fig. 7. Reconstructed images from the two consecutively recorded data sets whose bright-field images are shown in fig. 4. The magnitude greyscale (a and c) spans the range 0.8 to 1. The phase greyscale (b and d) spans the range −0.16 to 0.13. (a) Magnitude of reconstruction 1. (b) Magnitude of reconstruction 2. (c) Phase of reconstruction 1. (d) Phase of reconstruction 2.

because this indicates how strongly a particular spatial frequency was able to interfere with the unscattered beam. At points situated in the centres of the offset aperture functions, lens instability terms cancel (for reasons described below), and thus this gives, for a particular specimen, a relative measure of the source coherence function, assuming we have tested and removed the sampling errors described above. An absolute measure could be made if we calculate the strength of the specimen scattering function, which of course is implicit in the data itself: it may be obtained in principle by deconvolving the plane $G(r', 0)$, the conventional incoherent CBED pattern, with the intensity profile of the aperture function.

5. Double-resolution reconstruction

With reference to fig. 3a, we note that significant data has arrived in $G(r', \rho')$ at values of ρ' which are at twice the spatial frequencies of the maximum transfer which would normally arrive in the conventional bright-field image. We may think of this in terms of oblique incidence holography, via fig. 3b, in which case we observe that in tilted illumination a more extensive region of the Fraunhofer diffraction pattern of the specimen lying in the back-focal plane is passed through the usable region of the objective lens. Alternatively, we can think in terms of coherent convergent-beam electron diffraction (CBED), via figs. 3c and 3d. A particular periodicity in the specimen will scatter a diffracted disc to some point r'. As the probe is moved, there will be interference within the regions of overlap between this disc and the zero-order disc. If we observe the Fourier transform of the microdiffraction plane at the maximum value of ρ' where significant transfer occurs, we see information from scattered discs that lie in the CBED at up to twice the radius of the objective aperture. It should be emphasized that the data shown in fig. 6 is from an amorphous specimen; there is no actual crystalline disc observable in the diffraction plane. The sharply defined region merely indicates

where diffraction information corresponding to a particular spatial frequency has been expressed within the zero-order disc. The electrons which contributed to $G(r', \rho')$ for $|\rho'|$ close to 2α were scattered through an angle of 2α, and can thus provide information at twice the conventional resolution.

There are a number of ways we can obtain an improved resolution image from this data. The simplest is to note that along a line $\rho' = 2r'$ in $G(r', \rho')$, any symmetric phase changes across $A(r')$ such as defocus, astigmatism and spherical aberration cancel out, via the complex conjugates, at least beyond a third of the maximum value of ρ'. This is similar to noting that two-beam interference micrographs in CTEM, formed by passing the unscattered and scattered beam down opposite sides of the optic axis, are generally much easier to observe than genuine high-resolution contrast, because they are insensitive to the transfer function. In this case, however, because we have effectively measured all such pairs of beams, we can construct an estimate of $\Psi(r')$ by putting

$$\Psi(\rho') = G(\rho'/2, \rho'),   (9)$$

and then transforming back to give $\psi(r)$. Such reconstructions, from the two data sets for which the bright-field images are shown in fig. 4, are shown in fig. 7. The existence of aperture offset functions for ρ' vectors parallel to both the fast- and slow-scan directions is evidence of the consistency of the data sets, and the similarity between figs. 7a and 7b and figs. 7c and 7d demonstrates the reproducibility of the reconstruction. A more thorough use of the data, which uses all the scattered power in $G(r', \rho')$, while accounting for distortions in the objective lens, and which can also cope with the specimen being strongly scattering, is to Fourier-transform $G(r', \rho')$ with respect to r, forming $H(r, \rho')$, where it may be Wiener-filtered by a Wigner distribution dependent on $A(r')$, as described elsewhere [1–3]. For a weak phase object, the deconvolution effectively amounts to an integration of all scattered amplitude in the aperture offset functions after taking account of the phase across $A(r')$.

6. Conclusions

The actual resolution achieved in the reconstructions shown in fig. 7 (0.46 nm) is not particularly impressive compared to state-of-the-art high-voltage electron microscopes (typically 0.17 nm). The important thing to note, however, is that this resolution has been obtained with an optical arrangement which has a "conventional" resolution of only 0.93 nm, because we have used a relatively small objective aperture. We have also performed these experiments with a standard objective aperture (semi-angle of 8 mrad), which has a conventional resolution of 0.46 nm. This data can produce rather convincing double-resolution (0.23 nm) reconstructions. Consecutive experiments performed from the same region of specimen appear promisingly similar, but we refrain from publishing them here because they do not fulfill the self-consistency tests described above. The aperture features are definitely visible at some quite high values of $|\rho'|$ (see the example in fig. 8). In fig. 8 the phase shows the shape of the aperture overlap function more clearly; the π difference between the two parts (discussed earlier) can also be seen. The aperture overlap functions for other values of ρ' are often distorted and rarely occur in the directions parallel with the slow-scan direction of the probe. We infer, therefore, that we may have a significant component of accelerating drift, asymmetric tip instability in current or position, charging of the edge of the objective aperture or acoustic interference. We are presently attempting to discriminate these various components of error and eliminate them systematically. Indeed, it can be argued that the main strength of this method is that we can measure directly the self-consistency of the data in order to improve upon the instrumentation. Many other reconstruction methods do not allow for such tests, and may therefore sometimes give fallacious results. There is considerable room for improvement in our instrumentation, particularly in the water-cooling and air-conditioning of the microscope (which seriously affect drift), and in our recording medium (a TV-rate CCD camera), and so we interpret these first tests as extremely promising.
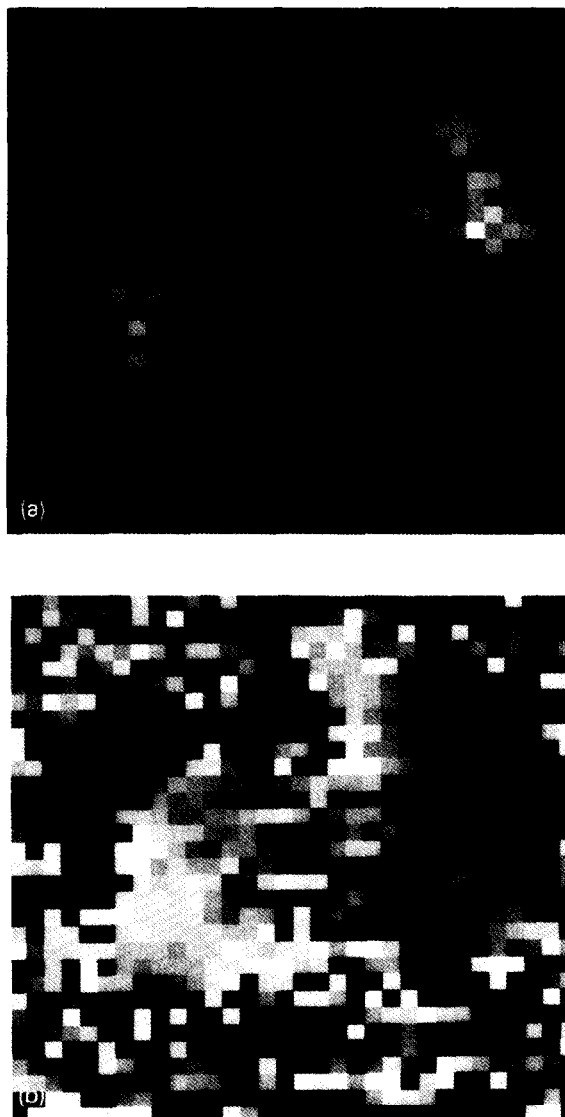

Fig. 8. A plot of $G(r', \rho')$ as a function of r' for a data-set recorded using the standard ($\alpha = 8$ mrad) objective aperture ($|\rho'| = 1.2\alpha$). (a) Magnitude. (b) Phase. The greyscale is in the range $-\pi$ to $+\pi$, so for a phase change across π the intensity of the plot changes abruptly. Note that corresponding points in the two parts of the aperture overlap function have a phase difference of π, since the specimen is weak phase; elsewhere the phase has random values. The phase change across each aperture overlap function can be explained by the effects of spherical aberration in the objective lens.

We believe that this method may offer the most robust route to sub-ångström-resolution electron microscopy. By processing only the bright-field (zero-order) disc of the microdiffraction plane, resolution can be doubled beyond the conventional information limit. For a strongly scattering specimen, the full Wigner distribution deconvolution allows, in theory, for the phasing of much higher-order diffracted amplitudes beyond the information limit, as has been demonstrated experimentally on the optical bench [4,5]. For strong, thick specimens, where appreciable Fresnel spreading occurs between different layers of the specimen, the multiplicative Fourier-optic description of the specimen and probe interaction (which leads to eq. (3)) breaks down. Under these circumstances, the addition of a holographic reference [17], or processing conventional images as a function of defocus [18] may be a better way to measure the phase of the exit wavefield. However, we note that given the constraint that the specimen is crystalline, the $\rho' = 0$ plane through $G(r', \rho')$, which is the integrated intensity in the microdiffraction plane from all probe positions and is equivalent to the conventional incoherent CBED pattern, should yield a unique solution of the complex scattering factors [19]. The information lying at $\rho' \neq 0$, which is equivalent to the coherent interference effects observed in CBED patterns (see, for example, ref. [20]), may therefore be processed using this method in order to remove the complications of the transfer of the objective lens, and thus create a much richer phase-sensitive data set, though one that will still have to be processed taking full account of dynamical scattering effects.

References

[1] R.H.T. Bates and J.M. Rodenburg, Ultramicroscopy 31 (1989) 303.
[2] J.M. Rodenburg and R.H.T. Bates, Phil. Trans. Roy. Soc. (London) A 339 (1992) 521.
[3] J.M. Rodenburg and B.C. McCallum, in: Proc. 10th Pfefferkorn Conf., 1992 (Scanning Microscopy International, AMF O'Hare, IL), in press.
[4] S.L. Friedman and J.M. Rodenburg, J. Phys. D (Appl. Phys.) 25 (1992) 147.
[5] B.C. McCallum and J.M. Rodenburg, Ultramicroscopy 45 (1992) 371.
[6] D. McMullan, J.M. Rodenburg and W.T. Pike, in: Proc. 12th Int. Congr. on Electron Microscopy, Seattle, 1990, Vol. 2, p. 104.
[7] O.L. Krivanek, Optik 45 (1976) 97.
[8] W. Hoppe and D. Köstler, in: Proc. 6th Eur. Congr. on Electron Microscopy, Jerusalem, 1976, Vol. 1 (TAL Int., Jerusalem, 1976) p. 99.
[9] D. Typke and D. Köstler, Ultramicroscopy 2 (1977) 285.
[10] A.J. Koster, W.J. de Ruijter, A. van den Bos and K.D. van der Mast, Ultramicroscopy 27 (1989) 251.
[11] K.-J. Hanszen, Adv. Electron. Electron Phys. 59 (1982) 1.
[12] M. Hohenstein, Ultramicroscopy 35 (1991) 119.
[13] M. Hohenstein, Appl. Phys. A 54 (1992) 485.
[14] J.M. Cowley, Diffraction Physics, 2nd ed. (North-Holland, Amsterdam, 1981).
[15] B.C. McCallum and J.M. Rodenburg, J. Opt. Soc. Am. A, in press.
[16] B.C. McCallum and J.M. Rodenburg, in: Proc. 10th Eur. Congr. on Electron Microscopy, Granada, 1991, in press.
[17] J.A. Lin and J.M. Cowley, Ultramicroscopy 19 (1986) 179.
[18] D. Van Dyck and W. Coene, Optik 77 (1987) 125.
[19] J.M. Zuo, J.C.H. Spence and R. Hoier, Phys. Rev. Lett. 62 (1989) 547.
[20] W.J. Vine, R. Vincent, P. Spellward and J.W. Steeds, Ultramicroscopy 41 (1992) 423.